Proceedings World Geothermal Congress 2026
Calgary, Canada, June 8 – 11, 2026

Micromechanics of Fluid-Induced Fault Reactivation From 4D X-Ray Microtomography

Birhanmeskel Woldemichael[1]*, Alexis Cartwright–Taylor[1,2], Elli-Maria Charalampidou[1], Nathaniel Forbes Inskip[1], Ian G. Main[2], Ian B. Butler[2], Michael Chandler[2], Xun Li[2], Maria-Daphne Mangriotis[3], Damien Freitas[4], Robert C. Atwood[5], Alexander Liptak[5]

[1]Heriot-Watt University, UK, [2]University of Edinburgh, UK, [3]National Oceanography Centre, UK, [4]University of Manchester at Harwell Science Campus, UK, [5]Diamond Light Source, UK

* bhw3000@hw.ac.uk

Keywords: Geothermal systems, Induced seismicity, Fault reactivation, Fluid injection, Micromechanics

INTRODUCTION

Geothermal systems are among the most promising sources of clean and renewable energy, offering both heat and electricity production, particularly in resource-limited regions (Kruszewski et al., 2023). However, during the operational lifetime of a geothermal reservoir, continuous fluid circulation can significantly alter the initial in-situ stress state. Variations in fluid pressure modify the effective normal stress acting on faults, potentially triggering slip and inducing seismicity (Buijze et al., 2019). For instance, in the Cerro Prieto geothermal field in Mexico, fluid injection has been associated with seismic events reaching magnitudes of approximately 5.0 Mw (Albores et al., 1980). Such occurrences raise concerns regarding the commercial viability of deep geothermal projects due to the associated geological and economic risks and their impact on the social and regulatory license needed for hydraulic stimulation and fluid extraction.

Previous laboratory experimental studies (e.g., Charalampidou et.al., 2015; Velcin et.al., 2020) have investigated the mechanisms of fluid-induced fault reactivation in both pre-existing and newly formed shear planes. Their results demonstrate that higher injection rates reduce nucleation length, leading to accelerated slip, larger fault displacements, and heightened seismic hazard. Furthermore, these experiments reveal that, during injection-induced reactivation, slip typically initiates along a pre-existing fault, after which a new, steeper fracture nucleate and progressively propagates. While such studies have valuable understanding of macroscopic fault behavior, they offer limited insight into the micromechanical processes governing strain localization, damage evolution, and fracture propagation during injection-induced reactivation.

At the field scale, induced seismicity is commonly managed using the “traffic-light” system, which regulates injection activities based on the maximum recorded event magnitude. However, this reactive approach is often insufficient, as intervention typically occurs only after thresholds are exceeded, leading to many examples of large ‘trailing events’ even after shut-down, such as deep heat mining Project in Basel, Switzerland (Häring et.al., 2008). On the other hand, more advanced strategies such as continuously adapting injection protocols in real time could more effectively mitigate seismic risk (Kwiatek et al., 2019; Mangriotis et al., 2025). Achieving this requires a mechanistic understanding of the small-scale deformation and damage processes driving fault reactivation, as well as their spatial and temporal evolution. Such insights are essential for developing predictive models capable of anticipating critical transitions that lead to larger seismic events.

This study investigates the impact of fluid injection on fault stability in laboratory rock deformation experiments to understand the micromechanics which lead to hydraulic fault reactivation and to evaluate the effectiveness of seismic event rate control in promoting stable, quasi-static failure during fluid injections. We combine in-situ fast synchrotron X-ray microcomputed tomography (μCT) with micro-seismic monitoring and control to characterize fault formation and reactivation. Internal deformation and microstructural evolution during progressive fault slip were captured using X-ray μCT and digital volume correlation (DVC). We quantified the volumetric and deviatoric strain fields. Our findings provide valuable insights into the effects of fluid injection in triggering fault slip and increased seismic hazard, and how this may be mitigated.

1 TESTING MATERIAL AND EXPERIMENT PROCEDURE

The tested material in this study is Clashach sandstone (Cartwright-Taylor et al., 2022) sourced from the Clashach Quarry in Morayshire, Scotland. This sandstone comprises over 92% quartz grains, less than 8% K-feldspar, and subordinate lithics. The granulometry of the rock is well-sorted with fine to medium-sized grains ranging from 0.25 to 0.4 mm in diameter.

The experiment was performed in a high-pressure X-ray transparent deformation apparatus named *Stór Mjölnir* (Cartwright-Taylor et al., 2022) which allows simultaneous monitoring of acoustic waves. The apparatus is built from titanium alloy, incorporating an X-ray transparent pressure vessel made of high-strength aluminum alloy, and allows real-time imaging of microstructural deformation using synchrotron μCT. It can reach confining pressures and axial stress up to 50 MPa and 500 MPa, respectively. *Stor Mjölnir* also features a hydraulic actuator and two piezoelectric compressional-wave transducers installed on top and bottom of the sample to monitor micro-seismicity and enable continuous feedback on the load based on the seismic response and hence stabilize deformation in the quasi-static rather than the unstable dynamic regime (Cartwright-Taylor et al., 2022; Mangriotis et al., 2025). The apparatus features a linear variable differential transformer (LVDT) to measure axial displacements; pressure sensors are used to monitor pressure applied by the hydraulic actuator and confining fluid and pore fluid within the sample.

Cylindrical samples with a diameter of 25 mm and a height of 10 mm were prepared using a thick-walled diamond core drill. Each rock sample was enclosed in a flexible silicone sleeve and placed in between a bottom platen and piston, whose outer diameter goes from 10 to 12 mm. After sample installation, and isotropic stress condition, where $\sigma_1 = \sigma_2 = \sigma_3$ and σ_i are the three principal components of the stress tensor, was achieved in a series of increments. First confining pressure, P_c, was increased to 10 MPa, then pore pressure, p, was increased to 5 MPa, then σ_3 and σ_1 were increased to 20 MPa to achieve zero effective differential stress at P_c = 25MPa and p = 5 MPa, where $\sigma_3 = P_c - p$.

The testing procedure consisted of three stages: quasi-static fault formation, unloading and hydraulic fault reactivation. During the quasi-static fault formation stage, differential stress was first increased from zero by initially applying axial load at a constant strain rate of 10^{-5} s^{-1}. Once acoustic emission (AE) events reached 1 event/s, continuous feedback control on axial load was switched to maintain a constant event rate and hence promote quasi static fault formation and shearing process whose evolution can be resolved by μCT analysis (Cartwright-Taylor et al, 2022). During the unloading stage, the previously generated fault was unloaded by decreasing the differential stress to 25 MPa. Then, in the third stage, the fault was reactivated by increasing the pore pressure at an injection rate of 18 μL/min while monitoring axial displacement and micro-seismicity. This was the first time reactivation was performed following controlled fault formation and unloading in such a cell.

X-ray microcomputed tomography scans, each consisting of 1801 X-ray projections with an exposure time of 0.05 s at different orientations through the sample, were collected throughout the experiment by rotating the apparatus at constant velocity on a stage using 70 keV monochromatic X-ray beam at Beamline I12-JEEP UK Diamond Light Source synchrotron. A total of 29 full 180° X-ray μCT scans were collected at various stages of the experiment, with each acquired in 90s. Subsequent reconstructions resulted in 3D X-ray tomographic volumes of 2774 × 2715 × 2715 voxels with voxel size of 7.918 microns voxel edge length. Black and dark grey values in these greyscale volumes correspond to high transmission (e.g. pore space) and lighter grey correspond to more absorptive grains of the sandstone. The 2D tomographic slices shown below were then obtained by taking cross sections along the eventual fault strike.

The internal deformation was quantified using digital volume correlation (DVC) performed between consecutive tomographic volumes with the open-source software SPAM (Stamati et al., 2020). In this approach, the reference and deformed μCT scan was divided into a grid of sub-volumes (in our case a 40-pixel node spacing), and local displacement vectors were calculated by finding the transformation that best maps each sub-volume from the reference image to its corresponding position in the deformed image. We then derived strain fields from the displacement data using a Q8 cubic element formulation, where the deformation gradient tensor (**F**) is evaluated at the center of each element. The right stretch tensor (**U**) is subsequently obtained by polar decomposition of **F**. Finally, volumetric strain is computed as the first invariant of the strain tensor as $J - 1$, while the deviatoric strain is computed as the second invariant of the strain tensor as $\left\| {}^{1}\!/\!_{J^{1/3}} \cdot \mathbf{U} \right\|$, where J is the determinant of **F**.

2 RESULTS

2.1 Macromechanical response

The mechanical response of Clashach sandstone in terms of the evolution of differential stress, AE event rate and pore pressure during the experiment is presented in Figure 1. The results are separated into three stages corresponding to the testing procedure. Stage 1 (quasi-static fault formation) starts under constant strain rate control with a small increase in the stress-time slope which is consistent with stiffening of the bulk sample by non-linear compaction between 10 to 32 MPa. Beyond this region, the differential stress increases quasi-linearly

reaching peak stress of 362.3 MPa. Meanwhile, the number of AE event rate initially averages less than 0.5 event/s until 50 minutes, when the sample reaches about 80% of the peak stress. As the AE event rate exceeded 1 event/s, the loading condition was switched to seismic response control to maintain that rate. The AE event rate increased rapidly at first, reaching 2 events/s at the peak stress, but then stabilized at 1AE/s thereafter. Nevertheless, AE feedback control succeeded in generating a prolonged phase of quasi-static sample failure.

Post peak the differential stress started to decrease implying a softening behavior, and consistent with the spontaneous emergence of a localized shear zone of tensile cracks (Fig 2c, Fig 3c lower diagram) with shear across the zone (Fig 3c upper), eventually resulting in the formation of a fault where two distinct blocks slide past one another along a shear plane with a visible offset on the sample boundary in Figures 2d,e,f. The AE event rate overall started to decrease during this phase, however there were intermittent episodes at which the event rate spiked to about 3 event/s. These stages could indicate when asperities in the shear plane were damaged, allowing for further shearing, although they could also be due to fluctuations in the statistical sampling of small numbers of events used in the feedback control.

During stage II the fault was unloaded by decreasing the differential stress to 25 MPa, to return the fault to a sub-critical state. The process lasted for about 30 minutes, resulting in a sudden decrease in the AE event rate to almost 0 event/s. In the last stage of the experiment, stage III, the fault was hydraulically reactivated by injecting water at rate of 18 µL/min. In Figure 1b, initially during injection ~0.13 minutes, the rate of pore pressure increase is slightly lower while differential stress curve shows that there is a temporary increase in stress of 5 MPa, consistent with an initial resistance to further slip. After this slip, the pore-pressure increase rate rose sharply, and the differential stress drops, consistent with stress relaxation enabled by a widening shear zone (Figs 2e,f and 3e,f) with greater implied permeability. The AE event rate also shows a local spike during this phase. The differential stress then remains constant for a period of 30 minutes until the pore pressure decreases back to its initial value of 5 MPa and then drops to a final value of 23.2 MPa.

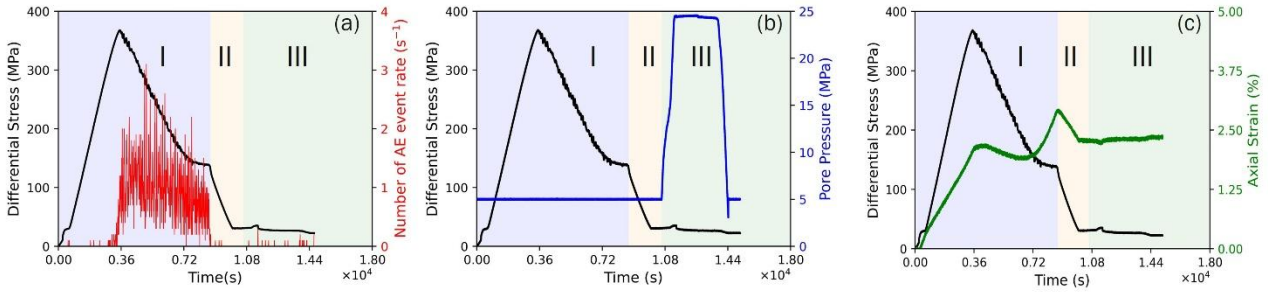


Figure 1. a) Evolution of differential stress (in black) and acoustic emission event rate (in red) with time. b) Differential stress and pore pressure (in blue) over time. c) Differential stress (MPa) and axial strain (%)

2.2 Micromechanical response

Vertical cross-sections of µCT images of Clashach sandstone deformation at various stages of the experiment are shown in Figure 2. The initial cross-section (Fig 2a), acquired at the beginning of deviatoric loading, shows a homogeneous sandstone with no pre-existing fractures. The following cross-section (Fig 2b), taken at peak stress, does not show any significant changes, even though the rock sample is experiencing an axial stress of 362.2 MPa and 2% axial strain. Fig 2c, captured during the strain-softening phase, shows the development of a localized shear zone propagating from the top right corner to the bottom left corner, accompanied by slight dilation due to en-echelon tensile cracking within the localized shear band.

Figures 2d, and 2e correspond to the unloading and the beginning of fluid injection. There are no significant differences observed between these two stages, indicating a distinct fault surface characterized by two separated blocks sliding past each other with greater dilation than that in the previous phase, due to fault opening displacement being required to overcome asperities generating the initial fault roughness visible on the images. Finally, Fig 2f, representing the end of the fluid injection phase, shows increased sliding along the fault plane, with dilation larger than at any of the earlier stages.

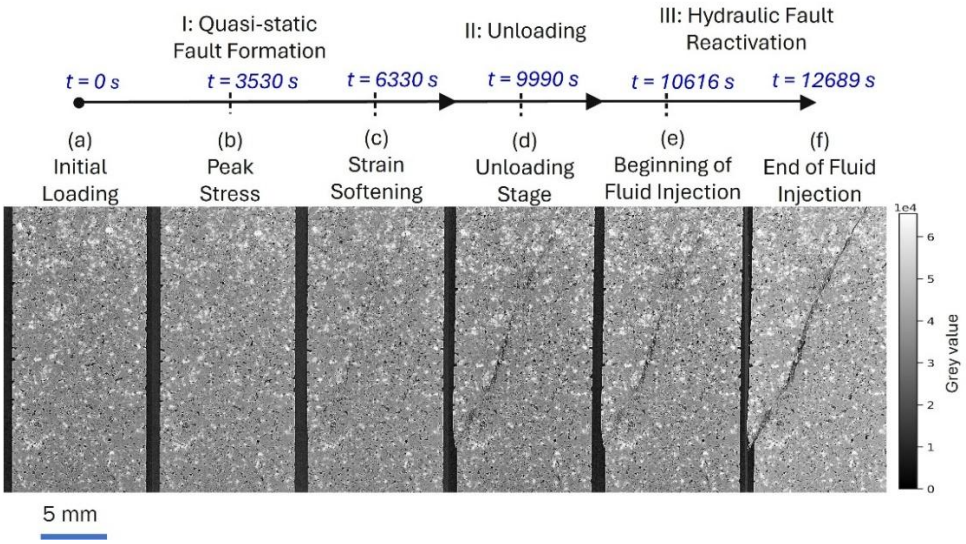


Figure 2. Vertical cross-sections (micro-computed tomographic slices) at different stages of the experiment, viewed along with the fault strike.

The strain fields in Fig 3 generally map well to the images they are based on in Fig 2, notably the shear and volumetric strain concentration in Fig 3c occurs where a visible fracture plane emerges during the strain-softening stage. However, at the peak stress stage, the strain field (Fig 3b) reveals an increase in both volumetric and shear strain that is not visible in the vertical X-ray cross-sections. This is due to the higher resolution of digital volume correlation, or interferometry in general, in detecting changes. The results confirm that the whole sample was compacting during the loading phase (Fig 3a). After the fault becomes visible between Figs 2c and 2f, dilation and shear were concentrated along the shear band while compaction continued away from the shearing plane (Fig 3c). No significant changes in the strain field were observed during unloading (Fig 3d) and the initial phase of fluid injection (Fig 3e). Figure 3f contains several contiguous pixels where it is not possible to resolve the shear strain (shown in black) or the volumetric strain (bright blue). This is consistent with the mechanical data, which show that acoustic emission (AE) activity began to spike only after some time had passed following the onset of fluid injection.

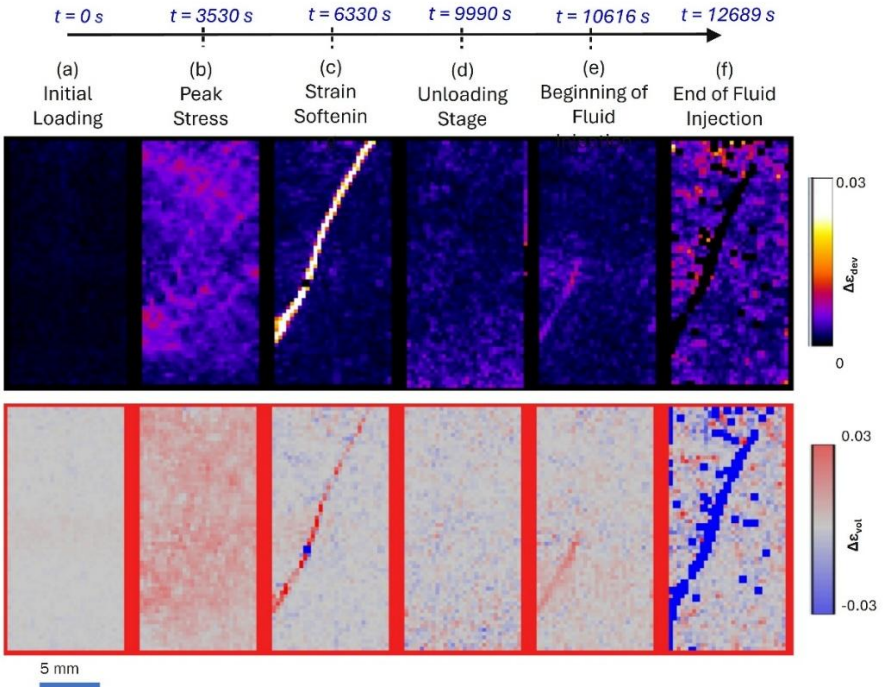


Figure 3. Shear and volumetric strain (dilation and compaction represented by red and blue respectively) at different stages of the experiment, unconverged pixels in (c) and (f) in black for deviatoric strain and blue color for volumetric strain

3 DISCUSSION AND CONCLUSION

The current study provides the first integrated view of fault reactivation and shear zone development during pore fluid injection by combining in situ X-ray μCT imaging with in-situ acoustic emission (AE) data. The results confirm that fault reactivation occurs at lower stresses than the initial fracture due to permanent weakening there, and that reactivation is enabled by dilation along the pre-existing shear band. The mechanical results are less obvious in showing the reactivation during fluid injection, whereas the results from DVC and μCT scans show sliding and dilation of the fault, whose effect on vertical strain may cancel each other out in the bulk axial strain measurement. The increase in AE event rate during fluid injection observed in this study is much lower than that reported in previous studies (Charalampidou et al., 2015; Velcin et al., 2020). We attribute these differences to the lower injected fluid volume applied in our study and the smaller sample size. Furthermore, while the earlier studies did not report any noticeable change in differential stress during fluid injection, the current results show a slight variation with an initial temporary increase followed by a subsequent more stable decrease. Future work will extend these observations to geothermal reservoir conditions, coupling fluid injection with acoustic emission monitoring and time-resolved X-ray tomography under controlled injection rates modulated to maintain a stable AE event rate. Such data will support predictive frameworks to optimize operations and mitigate micro seismicity.

REFERENCES

Albores, A., Reyes, A., Brune, J.N., Gonzalez, J., and Garcilazo, L.: Seismicity studies in the region of the Cerro Prieto geothermal field, *Geothermics*, **9**, (1980), 65–77.

Buijze, L., Bijsterveldt, L.V., Cremer, H., Paap, B., Veldkamp, H., Wassing, B.B., van Wees, J.-D., Yperen, G.C., Heege, J., and Jaarsma, B.: Review of induced seismicity in geothermal systems worldwide and implications for geothermal systems in the Netherlands, *Netherlands Journal of Geosciences*, **98**, (2019), e13.

Cartwright-Taylor, A., Mangriotis, M.-D., Main, I.G., Butler, I.B., Fusseis, F., Ando, E., Bell, A.F., Crippen, A., Rizzo, R.E., Marti, S., Leung, D.D., Curtis, A., and Magdsyuk, O.V.: Seismic events miss important kinematically governed grain-scale mechanisms during shear failure of porous rock, *Nature Communications*, **13**, (2022), 6169.

Charalampidou, E.-M.C., Stanchits, S., Kwiatek, G., and Dresen, G.: Brittle failure and fracture reactivation in sandstone by fluid injection, *European Journal of Environmental and Civil Engineering*, **19**(5), (2015), 564–579.

Häring, M.O., Schanz, U., Ladner, F., and Dyer, B.C.: Characterisation of the Basel 1 enhanced geothermal system, *Geothermics*, **37**, (2008), 469–495.

Kruszewski, M., Montegrossi, G., and Saenger, E.H.: The risk of fluid-injection-induced fault reactivation in carbonate reservoirs: an investigation of a geothermal system in the Ruhr region (Germany), *Geomechanics and Geophysics for Geo-Energy and Geo-Resources*, **9**, (2023), 38, 16 pp.

Kwiatek, G., Saarno, T., Ader, T., Bluemle, F., Bohnhoff, M., Chendorain, M., Dresen, G., Heikkinen, P., Kukkonen, I., Leary, P., Leonhardt, M., Malin, P., Martínez-Garzón, P., Passmore, K., Passmore, P., Valenzuela, S., and Wollin, C.: Controlling fluid-induced seismicity during a 6.1-km-deep geothermal stimulation in Finland, *Science Advances*, **5**, (2019), 7224.

Mangriotis, M.D., Cartwright-Taylor, A., Main, I.G., Curtis, A., Bell, A.F., Butler, I.B., and Fusseis, F.: Loading of a porous rock with constant micro-seismic event rate suppresses seismicity and promotes subcritical failure, *Scientific Reports*, **15**, (2025), 19351.

Stamati, O., Ando, E., Roubin, E., Remi, C., Wiebicke, M., Pinzon, G., Couture, C., Hurley, R.C., Caulk, R., Caillerie, D., Matsushima, T., Besuelle, P., Bertoni, F., Arnaud, T., Ortega Laborin, A., Rorato, R., Sun, Y., Tengattini, A., Okubadejo, O., Colliat, J.-B., Saadatfar, M., Garcia, F.E., Papazoglou, C., Vego, I., Brisard, S., Dijkstra, J., and Brimpilis, G.: SPAM: Software for Practical Analysis of Materials, *The Journal of Open Source Software*, **5**(51), (2020), 2286.

Velcin, H., Dautriat, J., Sarout, J., Esteban, L., and Godel, B.: Experimental reactivation of shear-fractured Berea and Boise sandstones by brine or liquid CO_2 injection at depth, *Journal of Geophysical Research: Solid Earth*, **125**, (2020), e2019JB018281.